A composite stochastic model considering the terrain topography for real-time GNSS monitoring in canyon environments

Zhetao Zhang[1,2], Yuan Li[1], Xiufeng He[1], Wu Chen[2], Bofeng Li[3]

1 School of Earth Sciences and Engineering, Hohai University, Nanjing 211100, China.
2 Department of Land Surveying and Geo-Informatics, The Hong Kong Polytechnic University, Hong Kong, China.
3 College of Surveying and GeoInformatics, Tongji University, Shanghai 200092, China.

Corresponding author

Xiufeng He (xfhe@hhu.edu.cn)

Abstract

The places of real-time Global navigation satellite system (GNSS) monitoring are usually located in a canyon environment, where the signals are frequently affected by multipath, diffraction, and even none-line-of-sight (NLOS) reception, etc. How to establish an accurate mathematical model is crucial at this time. In this paper, a composite stochastic model based on elevation, azimuth, and carrier-to-noise-power-density ratio (C/N_0) is proposed, which can reflect the terrain topography of the monitoring station. Specifically, according to a mapping function of azimuth, a so-called geographic cut-off elevation is introduced to detect and exclude the NLOS reception and even outlier, then a constrained elevation is obtained. Besides, based on the template functions of C/N_0 and its precision, a procedure is implemented to determine the equivalent elevation, where the contamination of multipath and diffraction are considered properly. To validate the effectiveness of the proposed method, a designed experiment and real deformation monitoring in canyon environments are both tested. The results show that the real terrain topography can be reflected to a great extent after using the proposed method. The positioning precision and reliability can be improved, and the performance of ambiguity resolution is also enhanced compared with the other traditional approaches. In real-time kinematic positioning, single-epoch centimeter-level and even millimeter-level accuracies can be obtained under these challenging conditions.

Keywords: Real-time GNSS monitoring; Stochastic model; Canyon environment; Elevation; Azimuth; C/N_0

1 Introduction

Global navigation satellite system (GNSS) has been widely used in areas of high-precision real-time monitoring including deformation monitoring, settlement monitoring, and structural health monitoring such as in landslides, dams, or bridges (Meng et al. 2007; Psimoulis et al. 2008; Liu et al. 2018). Since the places of GNSS monitoring are usually located in canyon environments like natural canyons and urban canyons. At this moment, the signals are frequently reflected, diffracted, and blocked, thus causing the multipath, diffraction, none-line-of-sight (NLOS) reception, outlier, etc. Hence, the prerequisite for achieving the GNSS high-precision and high-reliability positioning is to establish an accurate mathematical model including functional and stochastic models. Compared with the relatively more rigorous functional model that captures the relationship between the observations and unknown parameters, the stochastic model is more difficult to estimate where the precisions and correlations of observations need to be determined (Zumberge et al. 1997; Xu et al. 2007; Li 2016).

With the rapid development of multi-frequency and multi-constellation GNSS including the third generation of BeiDou Navigation Satellite System (BDS) (Yang et al. 2020), a subsequent question is how to accurately estimate the precisions of observations from different satellites and frequencies in real-time. The observation precisions are captured by the diagonal elements in a variance-covariance matrix. In the earlies stage, homoscedasticity was assumed where the precisions are assumed the same (Bischoff et al. 2005). This assumption is unrealistic since the signal quality and the systematic errors such as atmospheric effects from different observations are inevitably different. Accordingly, the assumption of heteroscedasticity becomes more popular. Two main indicators can reflect the signal quality to a great extent. The first one is the elevation since the systematic errors especially the atmospheric delays are more severe in the case of low elevations (Euler and Goad 1991; Li et al. 2017). The trigonometric and exponential functions can both be applied (King and Bock 1999; Dach et al. 2007; Amiri-Simkooei et al. 2009). The second one is the carrier-to-noise power density ratio (C/N_0) or signal-to-noise ratio (SNR) because the above indicators share the same tracking loops with the signals, thus indicating the high consistent with the signal quality (Talbot 1988; Axelrad et al. 1996). The exponential function with base 10 is the most famous and popular model (Brunner et al. 1999; Hartinger and Brunner 1999; Wieser and Brunner 2000). In addition, as a supplement, the variance component estimation can be used to optimize the variance factors of different observation types under different situations (Xu et al. 2006; Xu and Liu 2014). The minimum norm quadratic unbiased estimator (Rao 1971), the best invariant quadratic unbiased estimator (Koch 1978), and the least-squares variance component estimator are often adopted (Pukelsheim 1976).

Apart from the signal quality itself, the systematic error or the corresponding correction model is better considered in the stochastic model, especially when these error sources are not adequately addressed in the functional model. Several studies have been conducted on the effects of systematic errors. For instance, the atmospheric turbulence theory is applied to capture the atmospheric delays better (Schön and Brunner 2008a, b). A strategy based on C/N_0 is proposed to assign the appropriate weights for the affected observations caused by ionospheric scintillation (Luo et al. 2019). The Allan variance can also be used to analyze the stochastic characteristics especially in multi-source sensor positioning and navigation (Niu et al. 2014; Wang et al. 2018). The unmodeled effects also need to be taken into account, especially in a complex environment. The reason is that, at this time, the observation quality is often decreased, and the random characteristics may also be changed. Here the unmodeled error refers to the residual systematic error that cannot be eliminated

or easily mitigated by differencing and linear combination, empirical model correction, and proper parameterization (Li et al. 2018; Zhang et al. 2019). The unmodeled effects usually have temporal and spatial complexity, thus leading to cognitive limitations. The site-specific condition is one of the major factors causing the unmodeled effects, including the multipath, diffraction, and NLOS reception (Hofmann-Wellenhof et al. 2007; Hsu et al. 2015; Dong et al. 2016; Braasch 2017). To further reflect the true signal quality better in special cases, a more realistic cut-off elevation considering the azimuth can be used (Klostius et al. 2006; Atilaw et al. 2017). Several stochastic models have been proposed that consider the station environment, such as a new weighting model considering 3D mapping (Adjrad and Groves 2017). Also, a combination of multiple indicators is an effective approach including the combination of elevation and C/N$_0$ (Luo et al. 2014; Zhang et al. 2018b), the combination of elevation and azimuth (Han et al. 2018), or even the simple combination of elevation, azimuth, and SNR (Han et al. 2019).

Unfortunately, there is almost no systematic study on how to determine the observation weight that fully considers the station environment, such as the degrees of reflection, diffraction, and occlusion. This issue is rather crucial in high-precision GNSS monitoring especially when the monitoring station locates in a canyon environment. Because currently, the site-specific unmodeled errors (i.e., multipath, diffraction, and NLOS reception) are inevitably existent and even significant. In this study, we proposed a new stochastic model for estimating the appropriate observation precisions in real-time GNSS monitoring of a canyon environment. To validate the effectiveness of the proposed method, two types of experiments were carried out. The construction of azimuth mapping function and the determination of template function are both discussed. Then compared with the traditional methods, the positioning performance is analyzed comprehensively.

The main contribution of this paper is twofold. First, this study is the first to apply a composite stochastic model to fully consider the terrain topography of a monitoring station. Specifically, the proposed model considers the elevation, azimuth, and C/N$_0$ simultaneously, where the impacts of terrain topography are fully considered. Based on the traditional elevation, concepts of constrained elevation and equivalent elevation are proposed, which can reflect reality better. Second, we systematically study the mitigation of multipath, diffraction, NLOS reception, and even outlier based on the stochastic model compensation. Specifically, based on the elevation model, the azimuth is used to constrain the elevation where the terrain topographic factors are fully considered. In addition, the C/N$_0$ is applied to optimize the constrained elevation, where the impacts of abnormal signals are considered appropriately.

2 Methodology

In this section, the conventional stochastic models are given, then a composite stochastic model is proposed.

2.1 Three conventional stochastic models

The first traditional stochastic model is the equal-weight model, where the weighting scheme of GNSS observations is homoscedasticity. That is, the variance elements of code or phase observations are equal, which can be defined as follows (Bischoff et al. 2005)

$$\sigma^2_{equ} = c \tag{1}$$

where the σ_{equ} expresses the precision of undifferenced and uncombined GNSS observations according to the assumption of homoscedasticity; c denotes a constant coefficient.

The second stochastic model is the elevation-dependent model, of which the assumption of heteroscedasticity is adopted. The definition can be expressed as follows (Dach et al. 2007; King and Bock 1999)

$$\sigma_{ele}^2 = a/\sin^2(\theta) \tag{2}$$

where the σ_{ele} expresses the precision of undifferenced and uncombined GNSS observations based on the elevation θ; a denotes a constant coefficient. One additive constant coefficient can be added to (2) if necessary.

Another popular stochastic model is the C/N$_0$-dependent model, where the indicator of signal quality is used. The expression is as follows (Brunner et al. 1999; Hartinger and Brunner 1999)

$$\sigma_{snr}^2 = d \cdot 10^{-\frac{C/N_0}{10}} \tag{3}$$

where σ_{C/N_0} expresses the precision of undifferenced and uncombined GNSS observations based on the C/N$_0$; d denotes a constant coefficient. Similarly, one additive constant coefficient can be used if necessary.

2.2 A new composite stochastic model

The proposed composite stochastic model takes the topographical factors into account by combining the indicators of elevation, azimuth, and C/N$_0$ simultaneously. First, since the elevation model can fit the signal quality and atmospheric delays better than the equal-weight or C/N$_0$ in general (de Bakker et al. 2012; Zhang et al. 2018b), the elevation model is served as the fundamental model to reveal the basic precisions of the GNSS observations. Second, the azimuth is used to constrain the elevation, and a so-called constrained elevation can be obtained. Here the azimuth is used to describe the true terrain topography such as reflection, diffraction, and occlusion. It is worth noting that there may exist some obstacles that the signals are not influenced, such as the trees without leaves. Hence, it is necessary to judge whether the so-called obstacles need to be considered in real applications. In this study, thanks to the properties of C/N$_0$, it can be adopted to determine whether the signals are indeed influenced or not. Finally, the C/N$_0$ is applied to optimize the constrained elevation, thus obtaining the equivalent elevation. This is because the C/N$_0$ values are mainly influenced by the antenna gain, receiver, satellite transmitter, and path of signal spreading (Lau and Cross 2007). If the obstacles around the station are buildings, trees, or hills, the observed C/N$_0$ may deviate from the so-called template values. The template C/N$_0$ can be determined in advance in an ideal environment for a giving receiving system and satellite on a certain frequency (Strode and Groves 2016; Zhang et al. 2019). Therefore, the multipath, diffraction, and NLOS reception caused by the surrounding obstacles can be treated properly. Specifically, the proposed model can be expressed as follows

$$\sigma_{com}^2 = b/\sin^2\left(\bar{\theta}_{r,i}^s\right), \bar{\theta}_{r,i}^s \in (0, \pi/2] \tag{4}$$

where σ_{com} expresses the precision of undifferenced and uncombined GNSS observations based on the composite weighting scheme; b denotes a constant coefficient; $\bar{\theta}_{r,i}^s$ denotes the equivalent elevation for a certain receiving system r and satellite s on frequency i. Also, one additive constant coefficient can be added like (2) in reality.

As usual, there is a fixed natural cut-off elevation τ (e.g., $10°$) during GNSS data processing. This assumes that the surrounding observation environment is unobstructed. Apparently, this

assumption is often not realistic especially in areas of GNSS monitoring. In theory, there exists a concept of geographic cut-off elevation $\theta_{geo}(\omega_r^s)$, which is related to the azimuth

$$\theta_{geo}(\omega_r^s) = f(\omega_r^s), \omega_r^s \in [0,2\pi] \tag{5}$$

where $f(\omega_r^s)$ denotes a azimuth mapping function for a certain receiving system r and satellite s ω_r^s. Here, the geographic cut-off elevation captures the obstruction boundary. Hence, a more realistic cut-off elevation considering the terrain topography can be obtained if necessary

$$\tau' = \tau + \theta_{geo}(\omega_r^s) \tag{6}$$

Also, a constrained elevation can be estimated as follows

$$\bar{\theta}_{r,i}^s = \theta_{r,i}^s - \theta_{geo}(\omega_r^s) \tag{7}$$

It is worth noting that $\bar{\theta}_{r,i}^s$ may be zero or even negative when the NLOS reception happens. That is, the indirect signals from the obstructed satellite arrive at the receiver. Apparently, this type of $\bar{\theta}_{r,i}^s$ needs to be processed appropriately.

After that, the C/N$_0$ is used to refine the constrained elevation, and the equivalent elevation can be obtained. At first, in an ideal observation environment, template functions of C/N$_0$ and its standard deviation (STD) for a given receiving system and satellite on a certain frequency need to be determined. Take the cubic polynomial as an example, the template functions read (Zhang et al. 2019)

$$\text{C/N}_0^*(\theta_{r,i}^s) = \alpha_1 + \alpha_2 \times \theta_{r,i}^s + \alpha_3 \times \left(\theta_{r,i}^s\right)^2 + \alpha_4 \times \left(\theta_{r,i}^s\right)^3 \tag{8}$$

$$\text{STD}^*(\theta_{r,i}^s) = \beta_1 + \beta_2 \times \theta_{r,i}^s + \beta_3 \times \left(\theta_{r,i}^s\right)^2 + \beta_4 \times \left(\theta_{r,i}^s\right)^3 \tag{9}$$

where $\text{C/N}_0^*(\theta_{r,i}^s)$ and $\text{STD}^*(\theta_{r,i}^s)$ express the template C/N$_0$ and its STD when satisfying elevation $\theta_{r,i}^s$; α_1、α_2、α_3、α_4、β_1、β_2、β_3 and β_4 denote the coefficients to be determined. There are two main differences compared with the related existent studies about the template function. The first one is that the template functions in this study can be used even there is only one frequency, and the second one is that different template functions are determined based on different satellite types and receiver/antenna types for the first time. By comparing the template C/N$_0$ and observed C/N$_0$, the effects of obstacles will be evaluated, and the constrained elevation can be refined. Specifically, as aforementioned, there may exist significant differences between the observed C/N$_0$ and template C/N$_0$. Even if some signals have the same constrained elevation, the equivalent elevations may not be the same due to the different impacts from obstacles. Since the template C/N$_0$ can be regarded as normally distributed in case of a certain elevation interval, the probability density function of normal distribution can be applied. Then if we can have

$$\left|\text{C/N}_0(\bar{\theta}_{r,i}^s) - \text{C/N}_0^*(\bar{\theta}_{r,i}^s)\right| \leq k\text{STD}^*(\bar{\theta}_{r,i}^s) \tag{10}$$

where the k is a scale factor defined by the users, the constrained elevation is considered effective and can be used as an equivalent elevation. Otherwise, the constrained elevation needs to be adjusted as follows

$$\begin{cases} \bar{\theta}_{r,i}^s = \bar{\theta}_{r,i}^s - \delta, \text{C/N}_0(\bar{\theta}_{r,i}^s) \leq \text{C/N}_0^*(\bar{\theta}_{r,i}^s) \\ \bar{\theta}_{r,i}^s = \bar{\theta}_{r,i}^s + \delta, \text{C/N}_0(\bar{\theta}_{r,i}^s) > \text{C/N}_0^*(\bar{\theta}_{r,i}^s) \end{cases} \tag{11}$$

where δ is an adjustment constant that is related to the resolution of template functions. The equivalent elevation can be obtained with iteration by using the (11) or back-calculation directly based on the template functions. The scale factor k can be chosen according to the precisions of template functions and the actual situations. Actually, the proposed method is based on the idea of the three-segment processing. Specifically, the observations are excluded, or the weights of the observations are adjusted or maintained. Hence the proposed stochastic model is essentially a stochastic model compensation method focusing on the site-specific unmodeled errors and outliers simultaneously. The relationship between the various elevations mentioned above is shown in the Fig. 1. According to Fig. 1, the elevation in purple is the one calculated by the observation file and ephemeris file directly. The natural cut-off elevation in yellow is the fixed one set by the users in advance, such as $0°$, $10°$, or larger. The geometric cut-off elevation in green is the one that captures the obstruction boundary, which is related to the azimuth. The constrained elevation in blue is the one estimated from elevation minus geometric cut-off elevation. Then the equivalent elevation in red is the constrained elevation considering the degrees of reflection and diffraction.
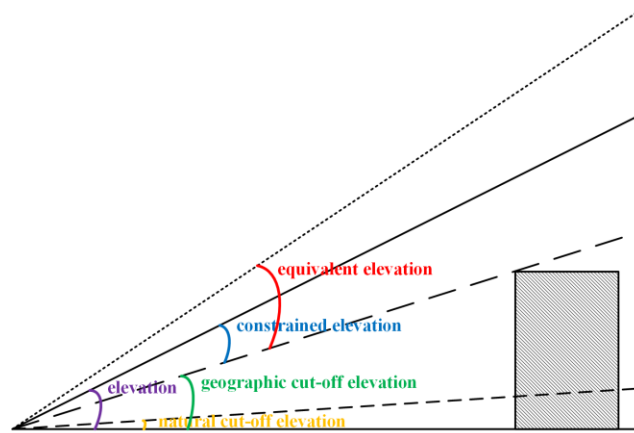

Fig. 1 Schematic diagram of elevation, natural cut-off elevation, geographic cut-off elevation, constrained elevation, and equivalent elevation

2.3 Real-time GNSS monitoring considering the terrain topography

Based on the above theory, a procedure for utilizing the proposed stochastic modeling method is summarized, which is shown in Fig. 2. It can be seen that there are preparatory issues and main processing steps in the proposed method.
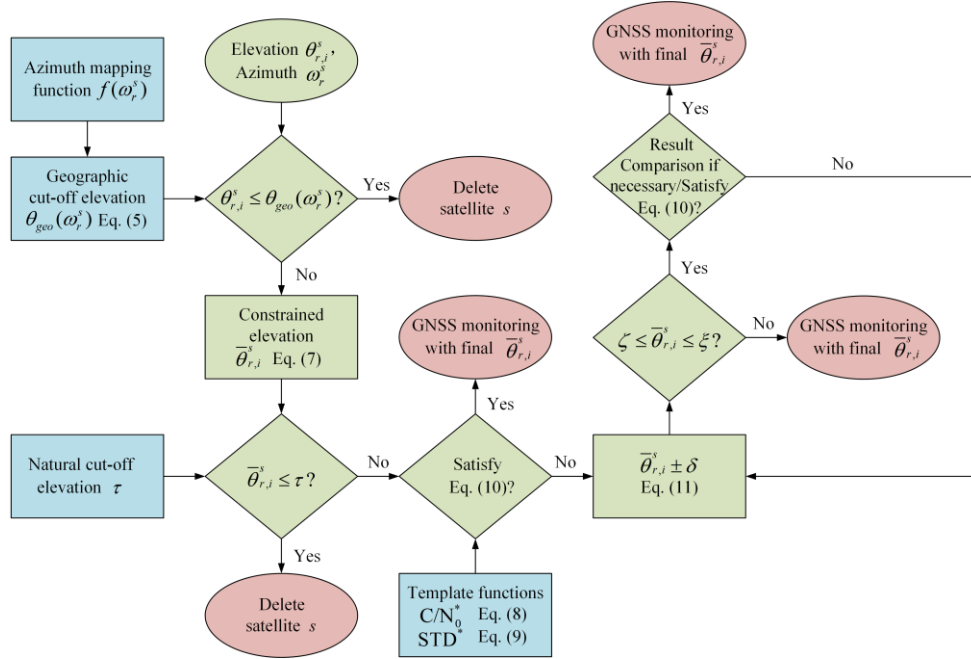
Fig. 2 Procedure of the composite stochastic model in real-time GNSS monitoring. The steps filled with blue, green, and red colors denote the preprocessing, processing, and ending, respectively

For the preparatory issues, there are two main issues.

(1) Construction of the azimuth mapping function

The data collection of azimuth mapping function $f(\omega_r^s)$ can rely on the digital elevation model, camera, or other measuring instruments including the total station and theodolite (Groves and Adjrad 2019). Based on this, the mapping function (5) can be generated and even fitted by spherical harmonics or higher-order polynomials, then the geographic cut-off elevation for a certain azimuth $\theta_{geo}(\omega_r^s)$ can be estimated.

(2) Determination of the template functions of C/N_0 and its precision

The sample C/N_0 data of a certain receiver can be collected under ideal conditions without occlusions. After the operations of quality control like the consistency check and minimum sample size test (Zhang et al. 2019), the specific template functions based on the satellite type classification can be determined. With the help of refined sample C/N_0 data (i.e., the nominal C/N_0), the template functions C/N_0^* and STD^* can be fitted with elevation-dependent functions, such as the cubic polynomials (8) and (9) suggested in this study. Finally, the template C/N_0 and its precision can be estimated according to a certain elevation.

The main processing steps are as follows.

(1) Comparison of the calculated elevation and geographic cut-off elevation

According to the calculated elevation $\theta_{r,i}^s$ and corresponding azimuth ω_r^s, the calculated elevation $\theta_{r,i}^s$ is compared with the geographic cut-off elevation $\theta_{geo}(\omega_r^s)$ with (5). If $\theta_{r,i}^s \leq \theta_{geo}(\omega_r^s)$, the signal from satellite s is regarded as the NLOS reception or outlier and then deleted. If $\theta_{r,i}^s > \theta_{geo}(\omega_r^s)$, the constrained elevation $\bar{\theta}_{r,i}^s$ is obtained with (7).

(2) Comparison of the constrained elevation and the natural cut-off elevation

The constrained elevation $\bar{\theta}_{r,i}^s$ is then compared with the natural cut-off elevation τ. If $\bar{\theta}_{r,i}^s \leq \tau$, the signal from satellite s is deleted. Otherwise, the $\bar{\theta}_{r,i}^s$ is used and entered into subsequent calculations.

(3) Check of the constrained elevation

With the help of template functions C/N_0^* and STD^*, the constrained elevation $\bar{\theta}_{r,i}^s$ is checked whether (10) is satisfied. If (10) is satisfied, the $\bar{\theta}_{r,i}^s$ is used directly. If (10) is not satisfied, the $\bar{\theta}_{r,i}^s$ needs to be adjusted.

(4) Estimation of the equivalent elevation

According to the constrained elevation and the observed C/N_0, the equivalent elevation can be estimated. In theory, one can back-calculate the equivalent elevation directly based on the template functions. There are two main reasons why the iteration is suggested. First, from a programming perspective, it is not an easy task for a computer to back-calculate directly the optimal equivalent elevation. Second, the result comparison may be adopted during the iteration if there are high-precision state equations in reality or observation residuals if necessary. Specifically, on the one hand, when there are available high-precision state equations, the new positioning results can be compared with the high-precision state equations. Actually, high-precision state equations are usually available, especially in long-term continuous monitoring. On the other hand, one can conduct the iteration based on the observation residuals. The iteration will be stopped if the difference in the results between two consecutive iterations is smaller than one certain threshold. Finally, the final constrained elevation is the equivalent elevation to be used. In this paper, iteration is suggested, where the estimation based on (11) can be stopped until when (10) is satisfied. After each adjustment of constrained elevation, the reasonableness of the adjusted constrained elevation needs to be checked, where ζ and ξ are the lower and upper bounds, respectively. Here, the cut-off elevation and 90 degrees are the lower and upper bounds, respectively.

Theoretically, two main factors enable the proposed method to work. The first one is the geographic cut-off elevation considering the azimuth, which can reflect the more realistic elevation and detect the NLOS reception and even outliers to a great extent. The second one is the template C/N_0 and observed C/N_0. With the help of template functions of C/N_0 and its precision, the properties between C/N_0 and site-specific unmodeled errors are fully taken into account. Then the degrees of reflection and diffraction can be evaluated with high precision and high reliability.

3 Results and discussion of designed experiment

In this section, a designed experiment was carried out. First, as an example, the mapping function of azimuth and template functions of C/N_0 and its STD were determined. Second, a field test of GNSS monitoring in a canyon environment was conducted.

3.1 Construction of azimuth mapping function

To apply the proposed stochastic model, the azimuth mapping function of monitoring station needs to be constructed previously. The monitoring station No. 1 is located on the Campus of Hohai University, Nanjing, China. Figs. 3 depicts the surrounding environments from north to south (up) and south to north (bottom) in the clockwise direction. It can be seen that the surrounding obstacles include the artificial and natural terrains simultaneously. Specifically, they are the buildings, trees with and without leaves, hills, etc. Hence, the multipath, diffraction, NLOS reception, and outlier may appear with high probabilities when conducting the real-time GNSS monitoring.

Fig. 3 Panoramas of monitoring station No. 1 from north to south (up) and south to north (bottom) in the clockwise direction

According to the terrain topography, the azimuth mapping function can be constructed. The geographic cut-off elevation can be determined by the mapping function for a given azimuth, where the theodolite is used in this study. The resolution of elevation is set to $0.01°$ due to the high-precision and high-reliability theodolite. Then since the template functions of STD of C/N_0 are established based on the 1-degree elevation interval, $1°$ is set as the resolution of azimuth. One can use other resolutions of azimuth and elevation according to the actual situation. Fig. 4 shows the sky mask of the monitoring station through a visual way according to the azimuth mapping function. The sky mask means the obstruction boundary projected on the skyplot for a certain position. It can be easily found that the boundaries of the high-rise and low-rise buildings, as well as the lush and sparse trees, are all included, where the geographic cut-off elevation ranges from $4.50°$ to $34.12°$. Therefore, the terrain topography contains the main features of the canyon environment and is representative.
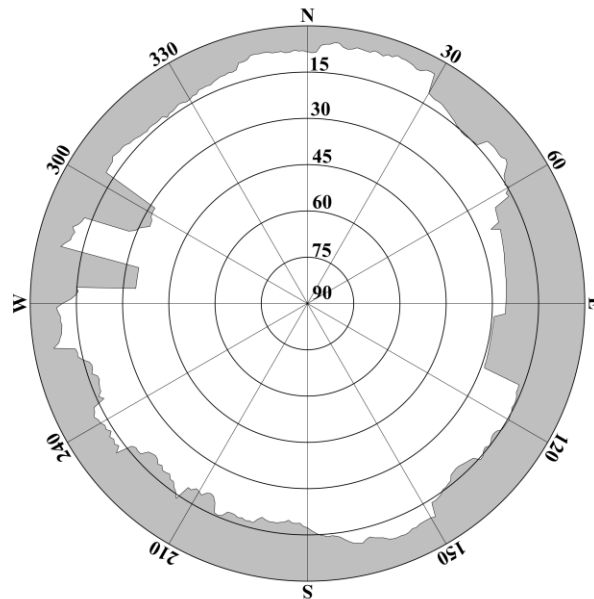

Fig. 4 Sky mask of monitoring station No. 1 according to the azimuth mapping function

3.2 Determination of template functions

In order to determine the template functions of C/N_0 and its precision, monitoring equipment No. 1 needs to be put in an ideal environment in advance, as shown in Fig. 5. The reason is that the template C/N_0 and its precision are rather stable and highly correlated with the elevation under the conditions of no occlusions. In this case, a high-end P5 receiver with antenna AT312 manufactured by CHCNAV is used. Then 24-h C/N_0 values with the sampling interval of 1 s were collected on the day of year (DOY) 13 in 2021. The frequencies of L1 (1575.42 MHz) and L2 (1227.60 MHz) in Global Positioning System (GPS), and B1 (1561.098 MHz) and B3 (1268.520 MHz) in BDS are all included.

Fig. 5 Monitoring equipment No. 1 in an ideal environment

To ensure high reliability when determining the template functions of C/N_0 and its STD. After consistency check and minimum sample size test, the sample C/N_0 data in the ideal environment is removed if the values exceed double STD ranges in a certain elevation interval (e.g., $1°$), where the confidence interval is 95%. Then the template functions (i.e., cubic polynomial) can be obtained according to the refined sample C/N_0 with the least-squares criterion.

For the P5 receiver, there is no universal template function after testing. Specifically, in the case of GPS, the observed C/N_0 behaviors of L1 and L2 are different. Also, the observed C/N_0 values of frequency L2 from the 8 IIR satellites are significantly lower than the ones from the other satellite types. The reason may be that the IIR satellites are launched earlier than any other satellites, thus indicating the relatively backward of the hardware. Hence, there are three types of template functions in the GPS: L1 from all the satellites, L2 except for the IIR satellites, and L2 from the IIR satellites. Fig. 6 shows the relationship between the elevation and nominal C/N_0 in the case of GPS. The fitted lines in these subplots denote the corresponding template functions of C/N_0.
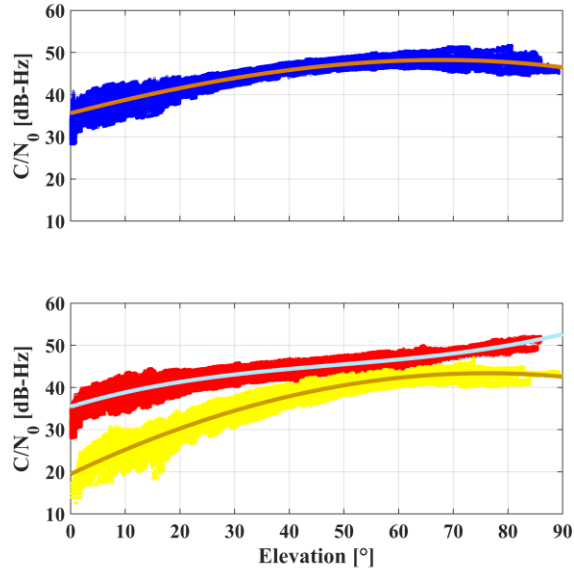
Fig. 6 Relationship between the elevation and nominal C/N_0 of GPS L1 (up) and GPS L2 (bottom) for monitoring equipment No. 1. The blue, red, and yellow points denote the L1 and L2 except for the IIR satellites, and L2 from the IIR satellites, respectively. The fitted lines with different colors denote the corresponding template functions of C/N_0

The corresponding template functions of C/N_0 and its STD are as follows

$$C/N_0^*\left(\theta_{r,\mathrm{L1}}^{\mathrm{G}}\right) = 35.61 + 0.332\theta_{r,\mathrm{L1}}^{\mathrm{G}} - 1.537 \times 10^{-3}\left(\theta_{r,\mathrm{L1}}^{\mathrm{G}}\right)^2 - 8.933 \times 10^{-6}\left(\theta_{r,\mathrm{L1}}^{\mathrm{G}}\right)^3 \quad (12)$$

$$\mathrm{STD}^*\left(\theta_{r,\mathrm{L1}}^{\mathrm{G}}\right) = 2.583 - 0.102\theta_{r,\mathrm{L1}}^{\mathrm{G}} + 1.763 \times 10^{-3}\left(\theta_{r,\mathrm{L1}}^{\mathrm{G}}\right)^2 - 8.557 \times 10^{-6}\left(\theta_{r,\mathrm{L1}}^{\mathrm{G}}\right)^3 \quad (13)$$

$$C/N_0^*\left(\theta_{r,\mathrm{L2}}^{\mathrm{EIIR}}\right) = 35.45 + 0.393\theta_{r,\mathrm{L2}}^{\mathrm{EIIR}} - 5.843 \times 10^{-3}\left(\theta_{r,\mathrm{L2}}^{\mathrm{EIIR}}\right)^2 + 3.995 \times 10^{-5}\left(\theta_{r,\mathrm{L2}}^{\mathrm{EIIR}}\right)^3 \quad (14)$$

$$\mathrm{STD}^*\left(\theta_{r,\mathrm{L2}}^{\mathrm{EIIR}}\right) = 2.157 - 0.0546\theta_{r,\mathrm{L2}}^{\mathrm{EIIR}} + 8.937 \times 10^{-4}\left(\theta_{r,\mathrm{L2}}^{\mathrm{EIIR}}\right)^2 - 5.101 \times$$
$$10^{-6}\left(\theta_{r,\mathrm{L2}}^{\mathrm{EIIR}}\right)^3 \quad (15)$$

$$C/N_0^*\left(\theta_{r,\mathrm{L2}}^{\mathrm{IIR}}\right) = 19.44 + 0.619\theta_{r,\mathrm{L2}}^{\mathrm{IIR}} - 3.863 \times 10^{-3}\left(\theta_{r,\mathrm{L2}}^{\mathrm{IIR}}\right)^2 - 1.815 \times 10^{-6}\left(\theta_{r,\mathrm{L2}}^{\mathrm{IIR}}\right)^3 \quad (16)$$

$$\mathrm{STD}^*\left(\theta_{r,\mathrm{L2}}^{\mathrm{IIR}}\right) = 3.317 - 0.0789\theta_{r,\mathrm{L2}}^{\mathrm{IIR}} + 1.105 \times 10^{-3}\left(\theta_{r,\mathrm{L2}}^{\mathrm{IIR}}\right)^2 - 5.778 \times 10^{-6}\left(\theta_{r,\mathrm{L2}}^{\mathrm{IIR}}\right)^3 \quad (17)$$

where $\theta_{r,\mathrm{L1}}^{\mathrm{G}}$, $\theta_{r,\mathrm{L2}}^{\mathrm{EIIR}}$ and $\theta_{r,\mathrm{L2}}^{\mathrm{IIR}}$ are the elevations of GPS L1, GPS L2 except for the IIR satellites, and GPS L2 from the IIR satellites, respectively.

In the case of BDS, the observed C/N_0 values are also different. Unlike the GPS, here the discrepancies only exist among different satellites. That is, the C/N_0 values of Medium Earth Orbit (MEO) satellites are generally higher than the ones of Inclined Geosynchronous Satellite Orbit (IGSO) satellites and Geostationary Earth Orbit (GEO) satellites. It is reasonable since the altitude of the MEO satellite orbit is lower than the one of the GEO or IGSO satellite. Hence the corresponding signal strength may be stronger more easily. There are two types of template functions in the BDS: B1/B3 from the MEO satellites, B1/B3 from the IGSO or GEO satellites. Fig. 7 illustrates the relationship between the elevation and nominal C/N_0 in the case of BDS. The fitted lines in these subplots denote the corresponding template functions of C/N_0.
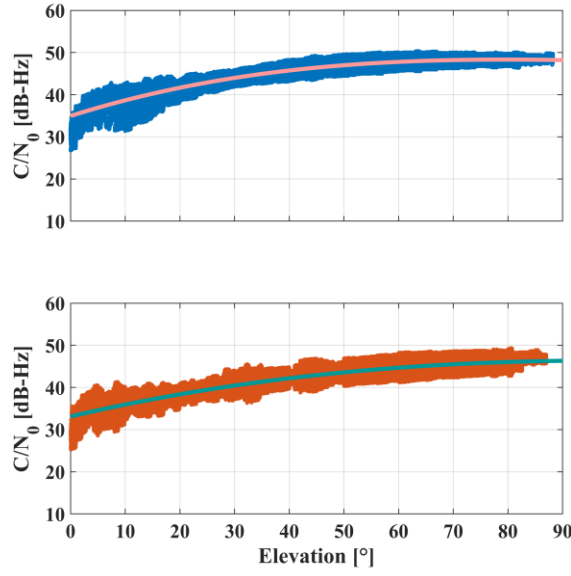
Fig. 7 Relationship between the elevation and nominal C/N$_0$ of BDS B1/B3 from the MEO satellites (up) and B1/B3 from the IGSO/GEO satellites (bottom) for monitoring equipment No. 1. The fitted lines with different colors denote the corresponding template functions of C/N$_0$

Similarly, the corresponding template functions of C/N$_0$ and its STD are as follows

$$C/N_0^*\left(\theta_{r,B13}^M\right) = 34.96 + 0.408\theta_{r,B13}^M - 3.931 \times 10^{-3}\left(\theta_{r,B13}^M\right)^2 + 1.143 \times 10^{-5}\left(\theta_{r,B13}^M\right)^3 \quad (18)$$

$$STD^*\left(\theta_{r,B13}^M\right) = 2.873 - 0.114\theta_{r,B13}^M + 2.316 \times 10^{-3}\left(\theta_{r,B13}^M\right)^2 - 1.527 \times 10^{-5}\left(\theta_{r,B13}^M\right)^3 \quad (19)$$

$$C/N_0^*\left(\theta_{r,B13}^{EM}\right) = 33.13 + 0.301\theta_{r,B13}^{EM} - 1.976 \times 10^{-3}\left(\theta_{r,B13}^{EM}\right)^2 + 2.957 \times 10^{-6}\left(\theta_{r,B13}^{EM}\right)^3 \quad (20)$$

$$STD^*\left(\theta_{r,B13}^{EM}\right) = 2.975 - 0.121\theta_{r,B13}^{EM} + 2.815 \times 10^{-3}\left(\theta_{r,B13}^{EM}\right)^2 - 1.947 \times 10^{-5}\left(\theta_{r,B13}^{EM}\right)^3 \quad (21)$$

where $\theta_{r,B13}^M$ and $\theta_{r,B13}^{EM}$ are the elevations of BDS B1 or B3 from the MEO satellites, and BDS B1 or B3 except for the GEO satellites.

According to Figs. 6 and 7, it can be clearly seen that the C/N$_0$ is positively correlated with the elevation. Hence the C/N$_0$ is also elevation-dependent. That is, any simple combinations of elevation and C/N$_0$ are not a very good choice since they are functionally overlapping. The better way to use C/N$_0$ is to utilize the template functions of C/N$_0$ and its precision, then the site-specific unmodeled errors can be detected by comparing the template C/N$_0$ and observed C/N$_0$ to a great extent.

3.3 Analysis of positioning performance

The experimental data of monitoring station No. 1 in the canyon environment were collected on the DOY 4 in 2021. The sampling rate is 1 Hz and the duration is approximately 2 hours, where

the GPS and BDS are all tested. Meanwhile, a nearby reference station in an ideal environment is also applied, and the baseline length is approximately 313.31 m, which is more consistent with the real monitoring applications. The main reason why the short baseline is usually applied in real-time monitoring is that the atmospheric delays can be considered eliminated in such harsh and high-precision scenes. The precise coordinates of the monitoring station are previously determined by precise point positioning (PPP) with the static solution.

The experiments are implemented by our self-developed software C-RTK (Canyon RTK), in which various special modules including cycle slip and data gap, multipath, outlier, and ambiguity resolution are all included. In this paper, the modules of cycle slip and outlier are used. Table 1 gives the detailed common processing strategies, including the information of functional and stochastic models. Specifically, since the outliers are very significant and cannot be totally eliminated in canyon environments, the method of detection, identification, and adaptation (DIA) based on the data snooping (Baarda 1968; Teunissen 2006) is adopted in advance. The method based on the robust estimation (Xu 1989; Yang et al. 2002) can also be applied although it partially overlaps with the proposed method. The approach of least-squares ambiguity decorrelation adjustment (LAMBDA) (Teuniseen 1995) is used, whereas this approach needs to be improved since the efficiency is not very fast (Xu 1998; Xu et al. 2012). Then in order to improve the efficiency of the ambiguity resolution, the modified LAMBDA (Chang et al. 2005) is adopted. The ratio is set to 3.0 in this experiment, of which the fixed rate is 96.8%. For the ionospheric delays, the Klobuchar model is used in advance, then the ionospheric delays can be regarded as eliminated after double differencing in such a short baseline, i.e., the ionosphere-fixed model. For ease of comparison especially when applying the azimuth, the natural cut-off elevation is $0°$. In order to fully validate the effectiveness of the proposed model, the real-time kinematic positioning (RTK) is used, where the result comparison is not adopted.

Table 1 Detailed common processing strategies

Item	Processing strategy
Used signals	GPS and BDS
Outlier preprocessing	DIA
Strategy of ambiguity resolution	LAMBDA
Correction of ionospheric delay	Ionosphere-fixed model
Correction of tropospheric delay	Saastamoinen model
Ratio of variance factors	Code:phase=10000:1

Then six types of stochastic models are applied and compared. The first three methods are the traditional ones, including (a) the equal-weight method (EQUM), (b) the elevation-dependent method (ELEM), and (c) the C/N_0-dependent method (CN0M). In order to validate the effectiveness of the geographic cut-off elevation and the template function, the fourth and fifth methods are the (d) the elevation-azimuth method (ELAM) like the method proposed by Han et al. (2018), and (e) the elevation-C/N_0 method (ELCN) in which the azimuth is not used. The ELAM and ELCN are actually the simplified forms of (f) the proposed composite method (COPM). In this case, we set the adjustment constant $\delta = 1°$, and the scale factor $k = 2$, thus having the 95% confidence level in theory.

First of all, the data quality of monitoring station No. 1 is analyzed with emphasis. Then the positioning results RTK are all discussed comprehensively. Fig. 8 illustrates the satellite numbers and position dilution of precision (PDOP) values of monitoring station No. 1, where the situations GPS, BDS, and GPS+BDS are all included. According to the top panel of Fig. 8, the satellite

number keeps changing during the session, thus indicating the signals are indeed affected frequently by the obstacles such as buildings, trees, hills, etc. Judging from the PDOP of Fig. 8, the values are almost larger than 1, and there exist some sudden fluctuations especially for the BDS, of which the value can reach nearly 6. It indicates that some satellites may be blocked and then the geometry deteriorates suddenly.
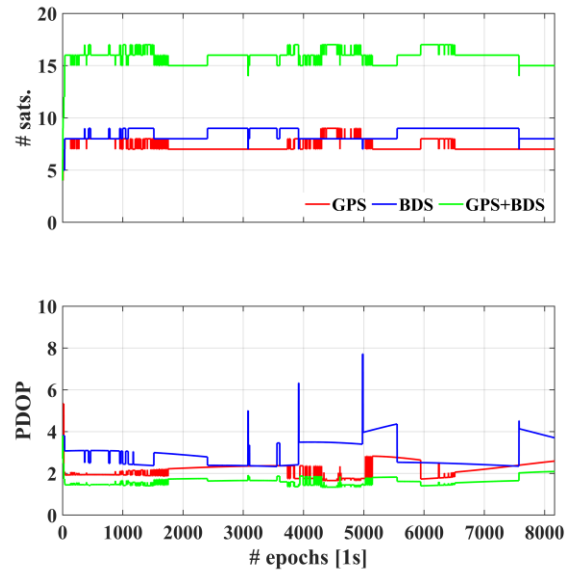

Fig. 8 Satellite numbers (top) and PDOP values (bottom) of monitoring station No. 1

Fig. 9 illustrates the observed C/N_0 values from the GPS and BDS of the monitoring station. Compared with the nominal C/N_0 shown in Figs. 6 and 7, the observed C/N_0 values are significantly different. Specifically, there are irregular fluctuations of the GPS C/N_0 from low elevations (approximately lower than 30°). For the BDS, the C/N_0 values of some MEO satellites are seriously attenuated of which the elevations locate between approximately 25° and 30°. Therefore, the results indicate that some signals may exist multipath, diffraction, NLOS reception, or even outlier. This also proves from the side that it makes sense to establish the template functions.
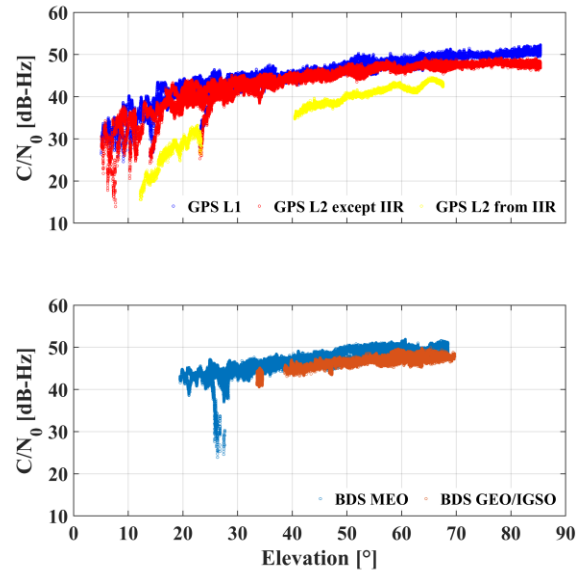
Fig. 9 Observed C/N$_0$ of monitoring station No. 1

Fig. 10 illustrates the RTK positioning errors compared with the reference values, where methods (a) to (f) are all included. The biases with blue, green, and red colors denote the ones in the east (E), north (N), and up (U) directions, respectively. The corresponding statistics including bias and root mean squared error (RMSE) are listed in table 2. Specifically, the biases in three directions of methods (a) to (f) are 0.89 cm, 0.60 cm, 0.64 cm, 0.59 cm, 0.58 cm, and 0.55 cm, respectively. The corresponding RMSE values are 2.67 cm, 2.02 cm, 2.06 cm, 1.83 cm, 1.66 cm, and 1.54 cm, respectively. According to the positioning results of the first three traditional methods (a) to (c), method (a) has relatively frequent large positioning results, and method (c) performs slightly worse than method (b) in general. It proves that the assumption of homoscedasticity is worse than the one of heteroscedasticity, and reasonable heteroscedasticity requires refinement. As for methods (d) and (e), the positioning results are improved compared with methods (a) to (c). It demonstrates that the azimuth in method (d) and C/N$_0$ in method (e) are both effective to some extent. Further improvement can be found in method (f). That is, compared with the other five methods, approximately 17.1% and 25.0% improvements of bias and RMSE in three dimensions can be obtained on average. It demonstrates the effectiveness of the proposed method, where the elevation together with azimuth and C/N$_0$ can reflect the true terrain topography with high efficiency. It is worth noting that in this experiment, method (e) performs slightly better than method (d). It tells us that the template functions of C/N$_0$ and its precision are rather important since they mainly focus on the multipath and diffraction which are the main major error sources in a canyon environment. In addition, some unstable or uncommon positioning results can be found like the positioning errors of method (f) in the U direction are smaller than the ones in the N direction. Actually, this phenomenon is widely existent in such canyon environments (Hsu et al. 2015; Groves and Adjrad 2019).
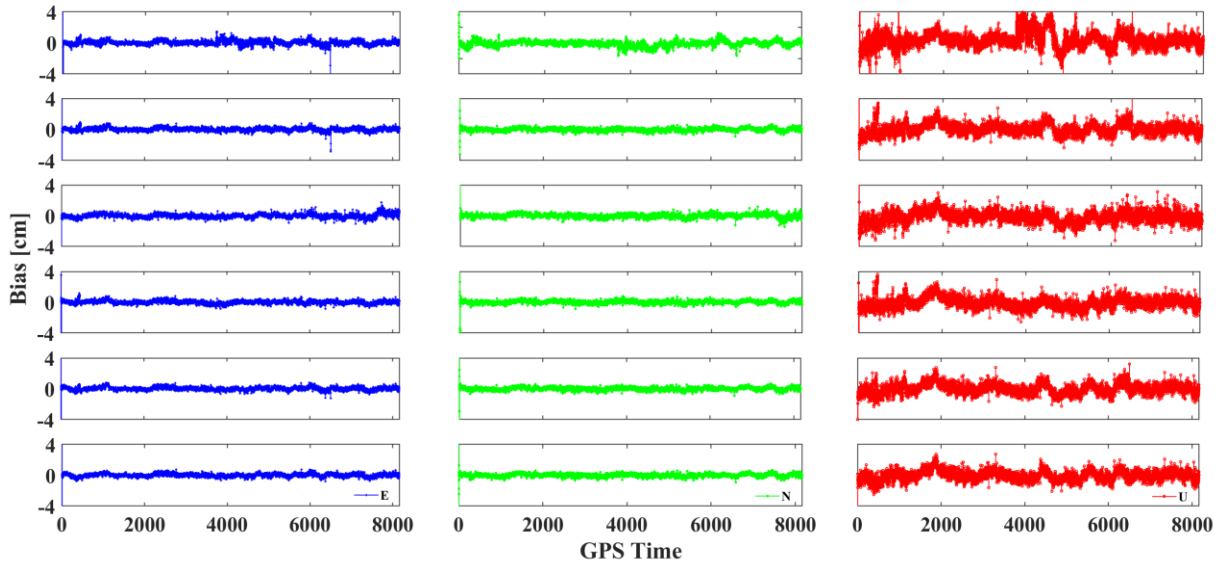
Fig. 10 RTK positioning results of monitoring station No. 1. The panels from top to bottom denote the results of methods EQUM, ELEM, CN0M, ELAM, ELCN, and COPM, respectively

Table 2 Statistics of monitoring station No. 1 with the methods EQUM, ELEM, CN0M, ELAM, ELCN, and COPM (unit: cm)

	Direction	EQUM	ELEM	CN0M	ELAM	ELCN	COPM
	E	0.237	0.175	0.199	0.190	0.184	0.168
Bias	N	0.272	0.164	0.199	0.161	0.162	0.160
	U	0.810	0.545	0.578	0.539	0.525	0.495
	E	0.827	0.733	0.750	1.185	0.910	0.732
RMSE	N	1.042	1.012	1.195	1.014	0.992	0.983
	U	2.318	1.587	1.505	0.957	0.967	0.927

In order to certify the necessity of introducing the equivalent elevation, as an example, Fig. 11 illustrates the double differenced (DD) residuals and elevations of G09 for monitoring station No. 1. The top and bottom panels denote the results of methods (a) and (f), respectively. According to the top panels, it can be seen that there is no significant relationship between elevations and residuals. Specifically, when the residuals are the largest at around the 4000th epochs, the elevations are not the lowest. It will certainly lead to unreasonable weight settings. However, this problem is alleviated to a great extent when the proposed method is conducted. The equivalent elevations are generally lower than the elevation most of the time, where the adjustment can reach approximately 5 degrees. In addition, the equivalent elevations from different frequencies may also be different, which is more resilient. Finally, the residuals become smaller and more random. Therefore, the elevations indeed need to be adjusted, and any single indicator cannot work all the time.
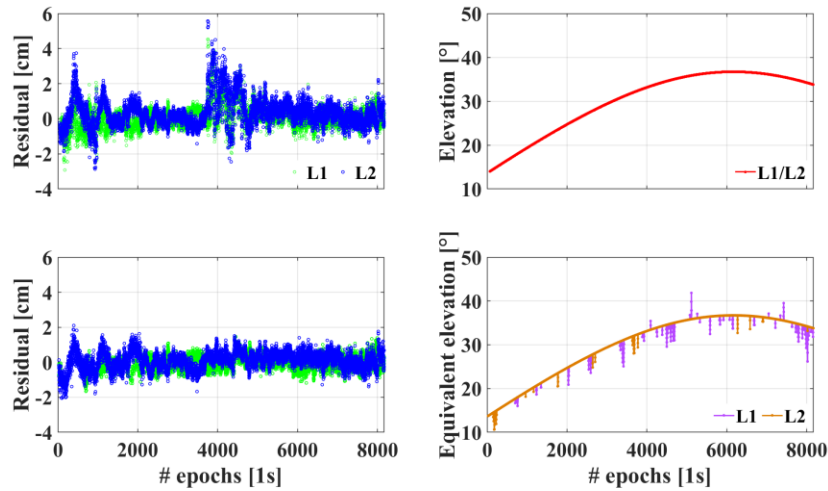
Fig. 11 DD residuals and elevations of satellite G09 for monitoring station No. 1. The top and bottom panels denote the results before (top) and after (bottom) using the proposed method, respectively

Fig. 12 illustrates the three-dimensional error distributions of RTK positioning results for monitoring station No. 1, and all six methods (a) to (f) are included. The positioning reliability can be evaluated according to the Fig. 12. It can be found that the first three traditional methods (a) to (c) have their advantages and disadvantages, where the elevation model is generally better than the other two methods. Then methods (d) and (e) are better than the traditional methods in general, thus indicating the effectiveness of the azimuth mapping function and template function. Also, when the azimuth and C/N_0 are both introduced, as shown in the results of method (f), the positioning results in terms of reliability are improved significantly. In conclusion, the proposed method is the most accurate in terms of precision and reliability and can reflect the real terrain topography accurately with high efficiency.
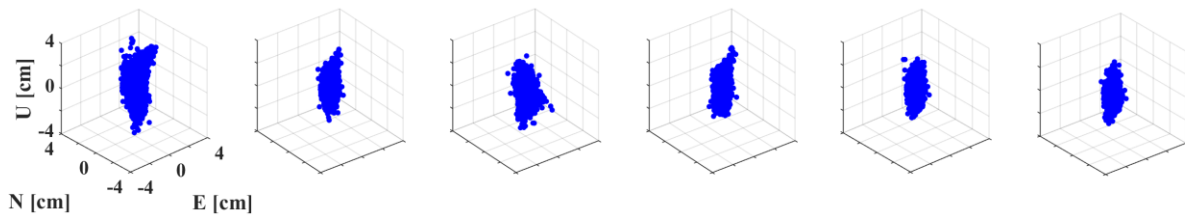

Fig. 12 Three-dimensional error distributions of RTK positioning results for monitoring station No. 1. The panels from left to right denote the results of methods EQUM, ELEM, CN0M, ELAM, ELCN, and COPM, respectively

4 Results and discussion of real monitoring data

In order to further validate the effectiveness of the proposed method, another dataset that is from the real deformation monitoring was applied and tested. Similarly, the mapping function of azimuth and template functions of C/N_0 and its STD were determined firstly. Then the results of real-time GNSS monitoring in a canyon environment are discussed.

4.1 Construction of azimuth mapping function

The receivers used in this section is a low-cost receiver manufactured by High Gain, named monitoring equipment No. 2. The model of this receiver is BX-RAG360, where the antenna and the GNSS board are integrated. The available frequencies are L1 (1575.42 MHz) and L2 (1227.60 MHz) for GPS, and B1 (1561.098 MHz) and B2 (1207.14 MHz) for BDS. The place of the real deformation monitoring station No. 2 is located in Huofeng Village, Bazhong, China. Once again, the azimuth mapping function can be constructed according to the terrain topography. The resolutions of azimuth and elevation are $1°$ and $0.01°$, respectively.

Fig. 13 shows the observed C/N_0 in terms of the sky plot for monitoring station No. 2, where different colors denote different C/N_0 values. It can be clearly seen that the west side of the station is blocked, especially in the southwest direction. Taking a closer look at the observed C/N_0 near the obstruction boundary, the values have different degrees of attenuation in different directions. The values vary from almost 15 to 55 dB-Hz. Since the lines are intermittent frequently at this time, the data gaps also happen. It demonstrates that the multipath, diffraction and NLOS reception are existent. In addition, we can find that the degrees of attenuation in different directions are quite different. This is most likely due to the different types of obstacles. This phenomenon indirectly proves that the azimuth alone cannot accurately measure the degrees to which the signals are affected by the site-specific unmodeled errors.
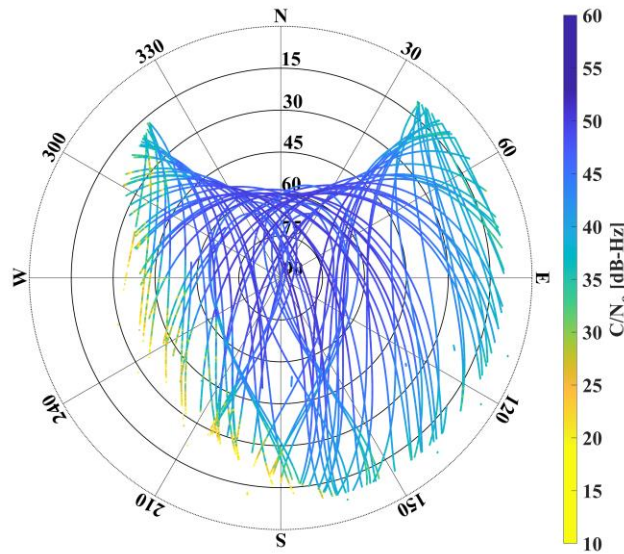

Fig. 13 Observed C/N_0 in terms of the sky plot for monitoring station No. 2

4.2 Determination of template functions

Since the receiver type and model are different from those in Section 3, the template functions need to be determined again. The monitoring equipment No. 2 is put in an ideal environment firstly. Fig. 14 illustrates the environment of monitoring equipment No. 2. Apparently, the unobstructed environment can be used to determine the template functions of C/N_0 and its precision. Since the low-cost types of antenna and board are adopted, the consequent question is whether there are systematic differences in C/N_0 behaviors for different receivers. Several receivers with the same model are put in the above same position consecutively. Fortunately, it is found that there are no systematic differences among different receivers with the same type, as shown in Figs. 15 and 16

below. It is consistent with the nature of the C/N$_0$, and it also demonstrates the feasibility of using the template functions for the low-cost receivers.

Fig. 14 Monitoring equipment No. 2 in an ideal environment

Similarly, 24-h C/N$_0$ values were collected. After conducting the consistency check and minimum sample size test, the sample C/N$_0$ data is removed when the values exceed double STD ranges within 1° interval. Finally, the template functions in the form of a cubic polynomial can be determined according to the refined sample C/N$_0$. Unlike monitoring equipment No. 1, There are a total of six template functions for monitoring equipment No. 2. Specifically, they are the L1, L2, B1 MEO, B2 MEO, B1 IGSO/GEO, and B2 IGSO/GEO. Figs. 15 shows the relationship between the elevation and nominal C/N$_0$ in the case of GPS. The fitted lines in these subplots denote the corresponding template functions of C/N$_0$. The reason why there is no need to separate the template functions of GPS L2 from different satellite types is that the low-cost receiver does not record L2 signals from IIR satellites for the purpose of low power consumption.
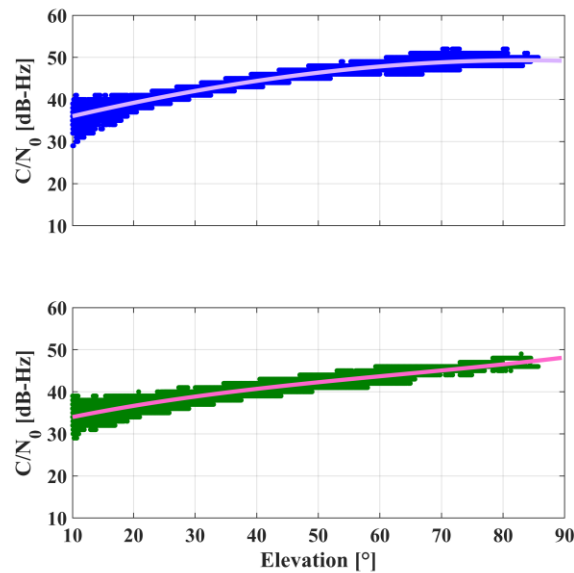

Fig. 15 Relationship between the elevation and nominal C/N$_0$ of GPS L1 (up) and GPS L2 (bottom) for monitoring equipment No. 2. The fitted lines with different colors denote the corresponding template functions of C/N$_0$

The corresponding template functions of C/N$_0$ and its STD are as follows

$$\text{C/N}_0^*(\theta_{r,\text{L1}}^\text{G}) = 32.45 + 0.373\theta_{r,\text{L1}}^\text{G} - 1.662 \times 10^{-3}(\theta_{r,\text{L1}}^\text{G})^2 - 4.602 \times 10^{-6}(\theta_{r,\text{L1}}^\text{G})^3 \quad (22)$$

$$\text{STD}^*(\theta_{r,\text{L1}}^\text{G}) = 3.872 - 0.207\theta_{r,\text{L1}}^\text{G} + 4.170 \times 10^{-3}(\theta_{r,\text{L1}}^\text{G})^2 - 2.549 \times 10^{-5}(\theta_{r,\text{L1}}^\text{G})^3 \quad (23)$$

$$\text{C/N}_0^*(\theta_{r,\text{L2}}^\text{G}) = 30.69 + 0.361\theta_{r,\text{L2}}^\text{G} - 3.512 \times 10^{-3}(\theta_{r,\text{L2}}^\text{G})^2 + 1.839 \times 10^{-5}(\theta_{r,\text{L2}}^\text{G})^3 \quad (24)$$

$$\text{STD}^*(\theta_{r,\text{L2}}^\text{G}) = 3.152 - 0.117\theta_{r,\text{L2}}^\text{G} + 2.107 \times 10^{-3}(\theta_{r,\text{L2}}^\text{G})^2 - 1.242 \times 10^{-5}(\theta_{r,\text{L2}}^\text{G})^3 \quad (25)$$

where $\theta_{r,\text{L2}}^\text{G}$ is the elevation of GPS L2. Compared with (12) to (15), according to the constant terms, it can be found that the template C/N$_0$ values from the low-cost receiver are lower than the ones from the high-end receiver. Also, the corresponding STDs from the low-cost receiver are larger than the ones from the high-end receiver. It is consistent with reality, thus indicating the rationality of the template functions.

Fig. 16 presents the relationship between the elevation and nominal C/N$_0$ of BDS B1 and B2 for monitoring equipment No. 2. Different colors denote different satellite and frequency types, and the fitted lines denote the corresponding template functions of C/N$_0$. The results are different from the previous scenes. That is, the discrepancies of template functions exist in both satellite and frequency types.
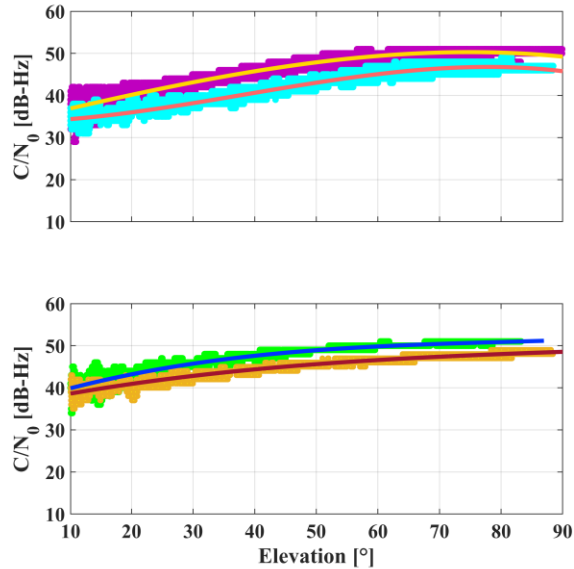

Fig. 16 Relationship between the elevation and nominal C/N$_0$ of BDS B1 (up) and BDS B2 (bottom) for monitoring equipment No. 2. The purple, cyan, green, and orange points denote the B1 MEO, B1 IGSO/GEO, B2 MEO, and B2 IGSO/GEO satellites, respectively. The fitted lines with different colors denote the corresponding template functions of C/N$_0$

Similarly, the corresponding template functions of C/N$_0$ and its STD are as follows

$$\text{C/N}_0^*(\theta_{r,\text{B1}}^\text{M}) = 33.48 + 0.346(\theta_{r,\text{B1}}^\text{M}) - 0.225 \times 10^{-3}(\theta_{r,\text{B1}}^\text{M})^2 - 1.854 \times 10^{-5}(\theta_{r,\text{B1}}^\text{M})^3 \quad (26)$$

$$\text{STD}^*(\theta_{r,\text{B1}}^\text{M}) = 3.726 - 0.150(\theta_{r,\text{B1}}^\text{M}) + 2.287 \times 10^{-3}(\theta_{r,\text{B1}}^\text{M})^2 - 1.067 \times 10^{-5}(\theta_{r,\text{B1}}^\text{M})^3 \quad (27)$$

$$\text{C/N}_0^*(\theta_{r,\text{B1}}^\text{EM}) = 33.66 + 0.0164(\theta_{r,\text{B1}}^\text{EM}) + 6.059 \times 10^{-3}(\theta_{r,\text{B1}}^\text{EM})^2 - 5.273 \times 10^{-5}(\theta_{r,\text{B1}}^\text{EM})^3 \quad (28)$$

$$\text{STD}^*\left(\theta_{r,\text{B1}}^{\text{EM}}\right) = 2.400 - 0.0837\left(\theta_{r,\text{B1}}^{\text{EM}}\right) + 1.666 \times 10^{-3}\left(\theta_{r,\text{B1}}^{\text{EM}}\right)^2 - 1.063 \times 10^{-5}\left(\theta_{r,\text{B1}}^{\text{EM}}\right)^3 \quad (29)$$

$$\text{C/N}_0^*\left(\theta_{r,\text{B2}}^{\text{M}}\right) = 35.57 + 0.478\left(\theta_{r,\text{B2}}^{\text{M}}\right) - 5.295 \times 10^{-3}\left(\theta_{r,\text{B2}}^{\text{M}}\right)^2 + 2.134 \times 10^{-5}\left(\theta_{r,\text{B2}}^{\text{M}}\right)^3 \quad (30)$$

$$\text{STD}^*\left(\theta_{r,\text{B2}}^{\text{M}}\right) = 4.450 - 0.215\left(\theta_{r,\text{B2}}^{\text{M}}\right) + 3.833 \times 10^{-3}\left(\theta_{r,\text{B2}}^{\text{M}}\right)^2 - 2.259 \times 10^{-5}\left(\theta_{r,\text{B2}}^{\text{M}}\right)^3 \quad (31)$$

$$\text{C/N}_0^*\left(\theta_{r,\text{B2}}^{\text{EM}}\right) = 35.82 + 0.303\left(\theta_{r,\text{B2}}^{\text{EM}}\right) - 2.585 \times 10^{-3}\left(\theta_{r,\text{B2}}^{\text{EM}}\right)^2 + 8.749 \times 10^{-6}\left(\theta_{r,\text{B2}}^{\text{EM}}\right)^3 \quad (32)$$

$$\text{STD}^*\left(\theta_{r,\text{B2}}^{\text{EM}}\right) = 2.394 - 0.0816\left(\theta_{r,\text{B2}}^{\text{EM}}\right) + 1.139 \times 10^{-3}\left(\theta_{r,\text{B2}}^{\text{EM}}\right)^2 - 5.079 \times 10^{-6}\left(\theta_{r,\text{B2}}^{\text{EM}}\right)^3 \quad (33)$$

where $\theta_{r,\text{B1}}^{\text{M}}$, $\theta_{r,\text{B1}}^{\text{EM}}$, $\theta_{r,\text{B2}}^{\text{M}}$, and $\theta_{r,\text{B2}}^{\text{EM}}$ are the elevations of B1 MEO, B1 IGSO/GEO, B2 MEO, and B2 IGSO/GEO satellites, respectively. Once again, by comparing the template functions of common satellite and frequency, i.e., (18) and (19) versus (26) and (27), we can find that the template C/N$_0$ values from the low-cost receiver are also lower than the ones from the high-end receiver according to the constant term. Then the corresponding STDs from the low-cost receiver are larger than the ones from the high-end receiver too. In conclusion, the template functions are rather reliable.

4.3 Analysis of positioning performance

24-h real deformation monitoring data of monitoring station No. 2 was tested, of which the observation date is the DOY 104 in 2021. Similarly, a nearby reference station is also applied, where the baseline length is 92.04 m. The receivers used in this section only outputs dual-frequency GPS and BDS observations with a sampling interval of 5 seconds. The reason is that the receivers for monitoring tend to be less expensive, and low power consumption and low latency are usually required in real-time monitoring. Due to the long-term continuous observation, the precise coordinates of the monitoring and reference stations are already known.

The experiments are also implemented by our self-developed software C-RTK. The common processing strategies are the same as the designed experiment, shown in Table 1. Setting a relatively high cut-off elevation is a feasible approach (Kaloop et al. 2020) in canyon environments although there may not be enough redundant observations. Since the observation condition of monitoring station No. 2 is worse than the one of monitoring station No. 1, different natural cut-off elevations and ratio values are used. Specifically, 10° is set as the natural cut-off elevation, and the ratio is 2.0 when conducting the ambiguity resolution. Actually, different experiments with different settings indirectly improve the persuasiveness of the proposed method. Also, six stochastic models are applied and compared, i.e., (a) EQUM, (b) ELEM, (c) CN0M, (d) ELAM, (e) ELCN and (f) COPM. Like the previously designed experiment, the adjustment constant and scale factor are set to 1° and 2, respectively.

Firstly, the data quality of monitoring station No. 2 is analyzed comprehensively. Fig. 17 depicts the satellite numbers and PDOP values of monitoring station No. 2. The results of GPS, BDS, and GPS+BDS are all included. It can be seen that the satellite numbers and PDOP values keep changing during the session. Specifically, the satellite numbers fluctuate around 20, where the satellite numbers of BDS are larger than the ones of GPS. For the PDOP, we can easily find that the PDOP values are almost larger than 1.5, especially for the GPS, where the PDOP values even rose violently to 17.1 at approximately 12:55. It indicates that the signals are indeed affected frequently and seriously by the around obstacles.
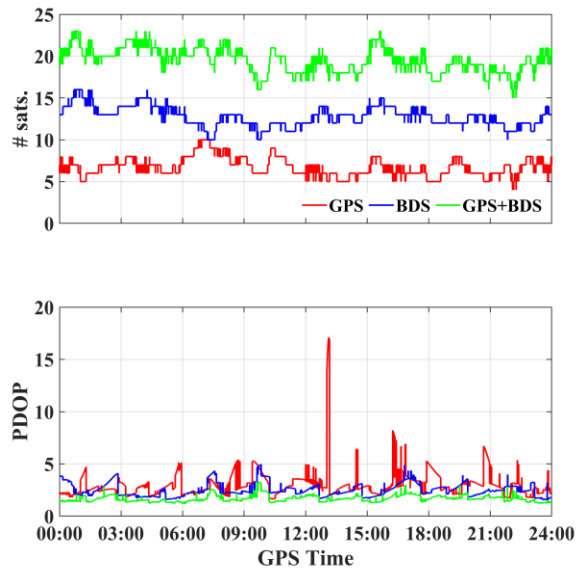
Fig. 17 Satellite numbers (top) and PDOP values (bottom) of monitoring station No. 2

Fig. 18 shows the observed C/N_0 values from the GPS and BDS of monitoring station No. 2. It can be easily seen that the observed C/N_0 are significantly different from the nominal C/N_0. Severe fluctuations especially the attenuation can be found regardless of the GPS or BDS. This abnormality can be found even when the elevations reach 60° or higher, of which the values can be as low as 20 dB-Hz or even smaller. Hence, it demonstrates that these signals exist lots of effects of multipath, diffraction, NLOS reception, and even outlier with high possibility. These signals need to be processed, otherwise it is impossible to obtain high-precision solutions in real time.
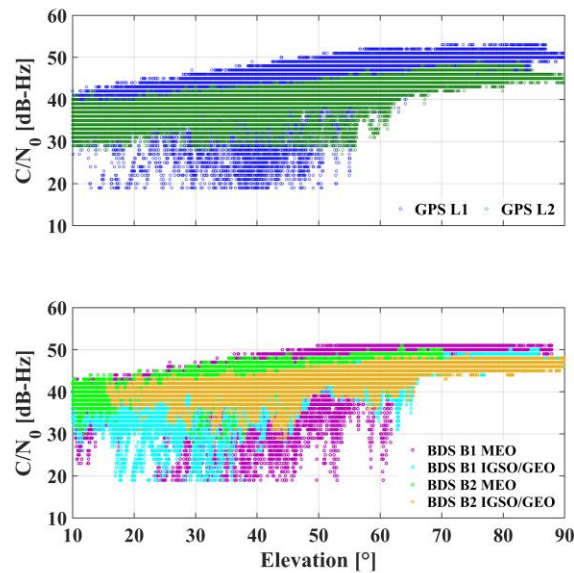

Fig. 18 Observed C/N_0 of monitoring station No. 2

Fig. 19 presents the RTK positioning errors compared with the reference values of monitoring station No. 2, where the solutions of three directions with methods (a) to (f) are all included. As a

supplement, the corresponding statistics are listed in Table 3. Specifically, the biases in three directions of methods (a) to (f) are 3.39 cm, 3.18 cm, 3.01 cm, 2.87 cm, 2.44 cm, and 2.05 cm, respectively. The corresponding RMSE values are 15.34 cm, 11.05 cm, 7.15 cm, 5.55 cm, 4.31 cm, and 2.89 cm, respectively. Based on the results, once again, method (a) has the worst positioning results. Then methods (d) and (e) are better than methods (b) and (c). The reason is that methods (d) and (e) consider the azimuth and C/N$_0$ respectively, although they may be not fully considered. Then take a closer look at the results of method (f), the positioning results have been greatly improved, where approximately 31.2% and 66.7% improvements can be obtained in terms of the bias and RMSE in three directions compared with the other five methods. Similar to the results of monitoring station No. 1, it is worth noting that there are no abnormal positioning results in the COPM. There are two main reasons. The first one is that the NLOS reception and outliers are rejected by the geographic cut-off elevation to a great extent, and the second one is that according to the template functions of C/N$_0$ and its precision, the degrees of reflection and diffraction are processed with high precision and high reliability. Therefore, it demonstrates that the introduction of geographic cut-off elevation and template function is very essential since they can reflect the obstruction of the monitoring environment to a great extent.
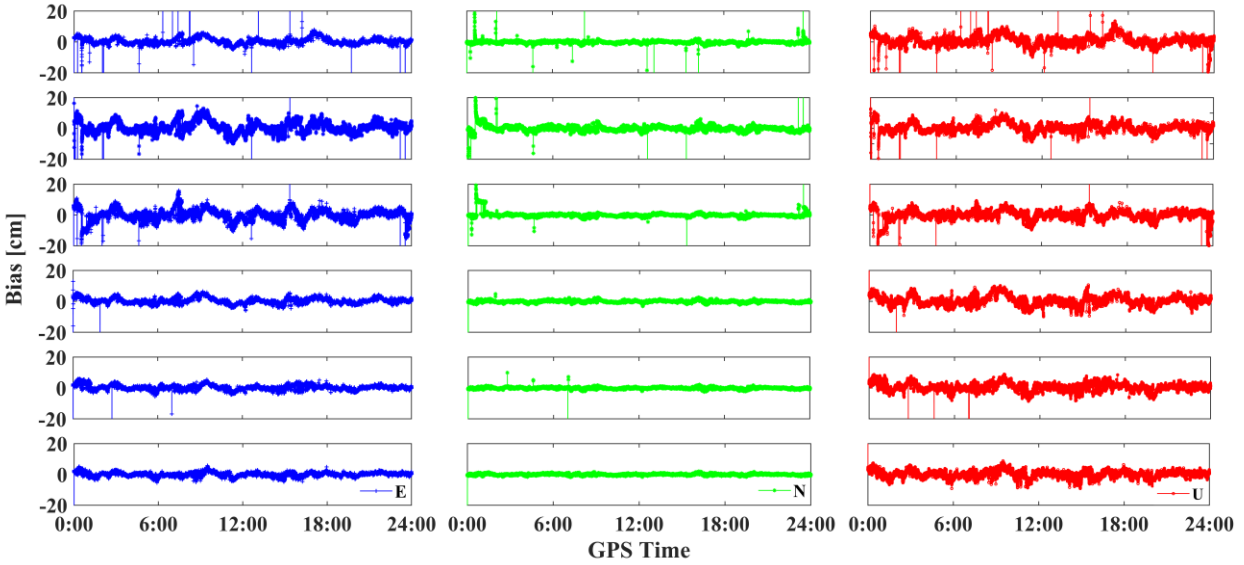

Fig. 19 RTK positioning results of monitoring station No. 2. The panels from top to bottom denote the results of methods EQUM, ELEM, CN0M, ELAM, ELCN, and COPM, respectively

Table 3 Statistics of monitoring station No. 2 with the methods EQUM, ELEM, CN0M, ELAM, ELCN, and COPM (unit: cm)

	Direction	EQUM	ELEM	CN0M	ELAM	ELCN	COPM
	E	1.715	1.575	1.441	1.432	1.225	0.983
Bias	N	0.659	0.781	0.866	0.556	0.443	0.369
	U	2.850	2.654	2.496	2.429	2.064	1.762
	E	6.069	4.734	2.679	1.910	1.841	1.499
RMSE	N	4.041	3.827	2.637	2.773	1.313	0.854
	U	13.497	9.217	6.083	4.406	3.666	2.316

To explore more evidence that the observation weights indeed need to be adjusted, the DD residuals and elevations of C08 for monitoring station No. 2 are shown in Fig. 20. The top and bottom panels denote the results of methods (a) and (f), respectively. It can be found again that the residuals are not dependent on the elevations all the time. Specifically, the second sharp fluctuation of the residuals does not correspond to a low elevation, of which the values are approximately 60°. Then for the results of method (f), the residuals become more consistent with the equivalent elevations. Moreover, according to the adjusted elevations, the adjustment amount can be up to almost 40 degrees. In conclusion, it is highly urgent to use the proposed method since it can adjust the observation weights adaptively instead of just relying on a single indicator.
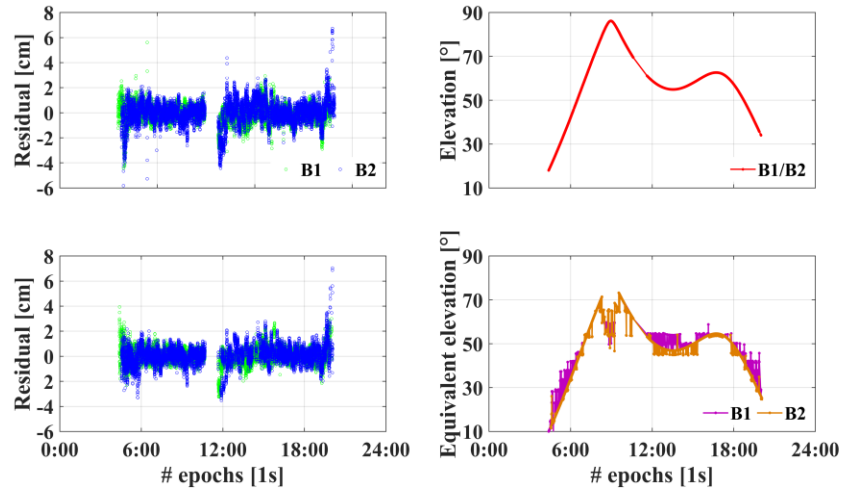

Fig. 20 DD residuals and elevations of satellite C08 for monitoring station No. 2. The top and bottom panels denote the results before (top) and after (bottom) using the proposed method, respectively

Fig. 21 depicts the three-dimensional error distributions of RTK positioning, where all the six methods (a) to (f) are included. The figures of three-dimensional distributions can reflect the overall performance better and more intuitively. Once again, it can be found that the error distributions of method (a) are the most discrete. Among the methods (a) to (e), methods (d) and (e) are better than any other three methods. Then for method (f), the results are much more accurate than any other method since the size of the error distributions is the smallest. The conclusions are consistent with the preceding analysis. That is, the proposed method can mitigate the site-specific unmodeled effects and outliers to a great extent.
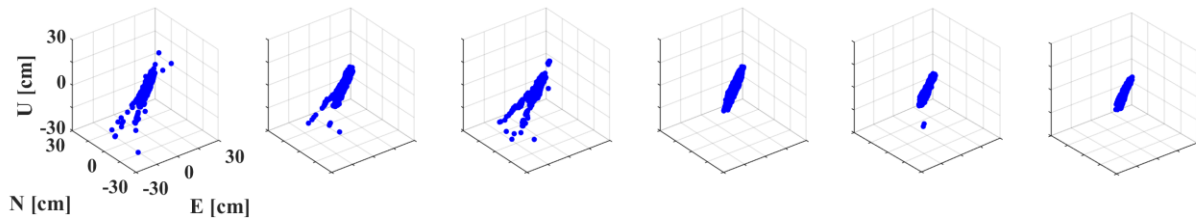

Fig. 21 Three-dimensional error distributions of RTK positioning results for monitoring station No. 2. The panels from left to right denote the results of methods EQUM, ELEM, CN0M, ELAM, ELCN, and COPM, respectively

Unlike monitoring station No. 1, the dataset in this section faces greater challenges, such as ambiguity resolution. Hence, the fixed rates are studied here. Table 4 lists the fixed rates of the six methods (a) to (f) under the conditions of different ratios. It indicates that the fixed rates of the proposed method are the highest regardless of the ratios. The fixed rates can still be higher than 70% and 58% even when the ratio equals 2 and 3, respectively. Overall, approximately 19.5% improvements can be obtained on average. This may be because the search space is changed and becomes more realistic after using the proposed method. In conclusion, the proposed can also improve the fixed rates of ambiguity resolution.

Table 4 Fixed rates of ambiguity resolution for monitoring station No. 2 with the methods EQUM, ELEM, CN0M, ELAM, ELCN, and COPM under different ratios (unit: %)

Ratio	EQUM	ELEM	CN0M	ELAM	ELCN	COPM
1.5	67.85	62.84	70.43	78.00	71.38	86.47
1.8	54.73	52.67	61.33	68.71	60.50	78.21
2.0	47.17	47.60	56.37	63.38	55.19	73.86
2.3	40.06	41.77	51.22	57.12	48.38	68.40
2.6	36.20	37.09	46.94	52.27	43.10	63.97
3.0	30.47	32.18	41.75	47.40	38.12	58.56

5 Conclusion

In this paper, we proposed a new stochastic model based on a composite indicator, including elevation, azimuth, and C/N_0. This method can reflect the terrain topography of real-time GNSS monitoring to a great extent. Hence, it is especially useful in a canyon environment, which has the characteristics of high occlusion and strong reflection. Two experiments were conducted to validate the effectiveness of the new stochastic model. Compared with the traditional equal-weight, elevation-dependent, and C/N_0-dependent models, as well as the composite stochastic model without the template function or mapping function, the proposed composite model has the best positioning performance, where single-epoch centimeter-level and even millimeter-level accuracies can be obtained. Moreover, approximately 17.1% to 31.2% and 25.0% to 66.7% improvements of bias and RMSE in three dimensions can be obtained on average. In addition, the fixed rates of ambiguity resolution can also be improved by approximately 19.5%. It demonstrates that the composite stochastic model can effectively mitigate the adverse effects of multipath, diffraction, NLOS reception, and even outlier.

In the future, the proposed method can be generated to the new composite stochastic model without azimuth or C/N_0 for simplicity. It may also be applied to other positioning modes, such as real-time PPP ambiguity resolution (i.e., PPP-AR) or even PPP-RTK, where the fractional cycle biases need to be estimated accurately. It can also be extended to multi-constellation and multi-frequency situations. Since the proposed method takes the form of an elevation model, it can be easily ported to the current GNSS positioning software.

Acknowledgments

Author contributions

ZZ proposed the idea, derived the formulae, developed the software, wrote the paper, and revised the manuscript. YL extended the program, worked out technical details, and revised the manuscript. XH designed the experiments and modified the manuscript. WC, BL supervised the study and modified the manuscript. All authors approved of the manuscript.

Data availability

The experimental data of this study are available from the corresponding author for academic purposes on reasonable request.

Conflict of interest

The authors have no competing interests to declare that are relevant to the content of this article.

References

Adjrad M, Groves P (2017) Enhancing Least Squares GNSS Positioning with 3D Mapping without Accurate Prior Knowledge: GNSS Positioning and 3D Mapping. Navigation 64:75–91

Atilaw T, Cilliers P, Martinez P (2017) Azimuth-dependent elevation threshold (ADET) masks to reduce multipath errors in ionospheric studies using GNSS. Adv Space Res 59:2726–2739

Amiri-Simkooei A, Teunissen P, Tiberius C (2009) Application of least-squares variance component estimation to GPS observables. J Surv Eng 135:149–160

Axelrad P, Comp C, Macdoran P (1996) SNR-based multipath error correction for GPS differential phase. IEEE Trans Aerosp Electron Syst 32:650–660

Baarda W (1968) A testing procedure for use in geodetic networks. In: Proceedings of Publications on geodesy

Bischoff W, Heck B, Howind J, Teusch A (2005) A procedure for testing the assumption of homoscedasticity in least squares residuals: a case study of GPS carrier-phase observations. J Geod 78:397–404

Braasch M (2017) Multipath. In: Springer Handbook of Global Navigation Satellite Systems. Springer, pp 443–468

Brunner F, Hartinger H, Troyer L (1999) GPS signal diffraction modelling: the stochastic SIGMA-Δ model. J Geod 73:259–267

Chang X, Yang X, Zhou T (2005) MLAMBDA: a modified LAMBDA method for integer least-squares estimation. J Geod 79:552–565

Dach R, Hugentobler U, Fridez P, et al (2007) Bernese GPS software version 5.0. Astron Inst Univ Bern 640:114

de Bakker P, Tiberius C, van der Marel H, van Bree R (2012) Short and zero baseline analysis of GPS L1 C/A, L5Q, GIOVE E1B, and E5aQ signals. GPS Solut 16:53–64

Dong D, Wang M, Chen W, et al (2016) Mitigation of multipath effect in GNSS short baseline positioning by the multipath hemispherical map. J Geod 90:255–262

Euler H, Goad C (1991) On optimal filtering of GPS dual frequency observations without using orbit information. Bull Géod 65:130–143

Groves P, Adjrad M (2019) Performance assessment of 3Dmapping–aided GNSS part 1: Algorithms, user equipment, and review. Navigation 66: 341-362

Han J, Huang G, Zhang Q, et al (2018) A New Azimuth-Dependent Elevation Weight (ADEW) Model for Real-Time Deformation Monitoring in Complex Environment by Multi-GNSS. Sensors 18:2473

Han J, Tu R, Zhang R, et al (2019) SNR-Dependent Environmental Model: Application in Real-Time GNSS Landslide Monitoring. Sensors 19:5017

Hartinger H, Brunner F (1999) Variances of GPS phase observations: the SIGMA-ε model. GPS Solut 2:35–43

Hofmann-Wellenhof B, Lichtenegger H, Wasle E (2007) GNSS–global navigation satellite systems: GPS, GLONASS, Galileo, and more. Springer Science & Business Media

Hsu L, Jan S, Groves P, Kubo N (2015) Multipath mitigation and NLOS detection using vector tracking in urban environments. GPS Solut 19:249–262

Kaloop M, Yigit C, El-Mowafy A, et al (2020). Evaluation of multi-GNSS high-rate relative positioning for monitoring dynamic structural movements in the urban environment. Geomatics, Nat Hazards Risk 11(1):2239-2262

King R, Bock Y (1999) Documentation for the GAMIT GPS analysis software. Mass Inst Technol Camb Mass

Klostius R, Wieser A, Brunner F (2006) Treatment of diffraction effects caused by mountain ridges. In: Proceedings of the 3rd IAG/12th FIG Symposium

Koch K (1978) Schätzung von varianzkomponenten. Allg Vermess Nachr 85:264–269

Lau L, Cross P (2007) Investigations into phase multipath mitigation techniques for high precision positioning in difficult environments. J Navig 60:457–482

Li B (2016) Stochastic modeling of triple-frequency BeiDou signals: estimation, assessment and impact analysis. J Geod 90:593-610

Li B, Zhang L, Verhagen S (2017) Impacts of BeiDou stochastic model on reliability: overall test, w-test and minimal detectable bias. GPS Solut 21:1095–1112

Li B, Zhang Z, Shen Y, Yang L (2018) A procedure for the significance testing of unmodeled errors in GNSS observations. J Geod 92:1171–1186

Liu N, Dai W, Santerre R, et al (2018) High Spatio-Temporal Resolution Deformation Time Series With the Fusion of InSAR and GNSS Data Using Spatio-Temporal Random Effect Model. IEEE Trans Geosci Remote Sens 57:363-380

Luo X, Gu S, Lou Y, et al (2019) Better thresholds and weights to improve GNSS PPP under ionospheric scintillation activity at low latitudes. GPS Solut 24:17

Luo X, Mayer M, Heck B, Awange J (2014) A Realistic and Easy-to-Implement Weighting Model for GPS Phase Observations. IEEE Trans Geosci Remote Sens 52:6110–6118

Meng X, Dodson A, Roberts G (2007) Detecting bridge dynamics with GPS and triaxial accelerometers. Eng Struct 29:3178–3184

Niu X, Chen Q, Zhang Q, et al (2014) Using Allan variance to analyze the error characteristics of GNSS positioning. GPS Solut 18:231–242

Psimoulis P, Pytharouli S, Karambalis D, Stiros S (2008) Potential of Global Positioning System (GPS) to measure frequencies of oscillations of engineering structures. J Sound Vib 318:606–623

Pukelsheim F (1976) Estimating variance components in linear models. J Multivar Anal 6:626–629

Rao C (1971) Estimation of variance and covariance components MINQUE theory. J Multivar Anal 1:257–275

Schön S, Brunner F (2008a) Atmospheric turbulence theory applied to GPS carrier-phase data. J Geod 82:47–57

Schön S, Brunner F (2008b) A proposal for modelling physical correlations of GPS phase observations. J Geod 82:601–612

Strode P, Groves P (2016) GNSS multipath detection using three-frequency signal-to-noise measurements. GPS Solut 20:399–412

Talbot N (1988) Optimal weighting of GPS carrier phase observations based on the signal-to-noise ratio. In: Proceedings of the International Symposia on Global Positioning Systems

Teunissen P (1995) The least-squares ambiguity decorrelation adjustment: a method for fast GPS integer ambiguity estimation. J Geod 70:65–82

Teunissen P (2006) Testing theory: an introduction, 2nd edn. Delft University Press

Wang D, Dong Y, Li Q, et al (2018) Using Allan variance to improve stochastic modeling for accurate GNSS/INS integrated navigation. GPS Solut 22:53

Wieser A, Brunner F (2000) An extended weight model for GPS phase observations. Earth Planets Space 52:777–782

Xu P (1989) On robust estimation with correlated observations. Bull. Geodesique 63:237–252

Xu P (1998). Mixed Integer Geodetic Observation Models and Integer Programming with Applications to GPS Ambiguity Resolution. J Geod Soc Jpn 44:169–187

Xu P, Liu J (2014) Variance components in errors-in-variables models: estimability, stability and bias analysis. J Geod 88, 719–734

Xu P, Liu Y, Shen Y, Fukuda Y (2007) Estimability analysis of variance and covariance components. J Geod 81:593–602

Xu P, Shen Y, Fukuda Y, Liu Y (2006) Variance component estimation in linear inverse ill-posed models. J Geod 80:69–81

Xu P, Shi C, Liu J (2012) Integer estimation methods for GPS ambiguity resolution: an applications oriented review and improvement, Surv Rev 44:59–71

Yang Y, Mao Y, Sun B (2020) Basic performance and future developments of BeiDou global navigation satellite system. Satell Navig 1:1-8

Yang Y, Song L, Xu T (2002) Robust estimator for correlated observations based on bifactor equivalent weights. J Geod 76, 353–358

Zhang Z, Li B, Gao Y, Shen Y (2019) Real-time carrier phase multipath detection based on dual-frequency C/N0 data. GPS Solut 23:7

Zhang Z, Li B, Shen Y, et al (2018b) Site-Specific Unmodeled Error Mitigation for GNSS Positioning in Urban Environments Using a Real-Time Adaptive Weighting Model. Remote Sens 10:1157.

Zhang Z, Li B, Shen Y, Yang L (2017) A noise analysis method for GNSS signals of a standalone receiver. Acta Geod Geophys 52:301–316

Zumberge J, Heflin M, Jefferson D, et al (1997) Precise point positioning for the efficient and robust analysis of GPS data from large networks. J Geophys Res Solid Earth 102:5005–5017